INVITED FEATURE ARTICLE

# A critical evaluation of indentation crack lengths in air

## Robert F. Cook 🔘

Materials Measurement Science Division,
National Institute of Standards and
Technology, Gaithersburg, MD, USA

**Correspondence**
Robert F. Cook, Materials Measurement
Science Division, National Institute of
Standards and Technology, Gaithersburg,
MD 20899, USA.
Email: robert.cook@nist.gov

**Abstract**

An extensive overview is presented of Vickers indentation crack lengths in ceramics in air. Measurement of such crack lengths is one of the most common and powerful assessments of the fracture properties of ceramics and the overview provides a critical evaluation of observed behavior as functions of material type and indentation load, and an extensive basis for comparison of results from new materials and analyses. The overview considers single crystals, polycrystals, transforming materials, glasses, and multiphase materials, including cermets, glass-ceramics, and tooth enamel. The coverage extends over structural and electronic ceramics, including oxides, carbides, nitrides, and titanates. The data are presented in a single format for ease of interpretation in terms of idealized indentation fracture and for inter-material comparisons; most data are unique to this work, but the results of selected studies from the published literature are included. The overview considers the precision and accuracy of crack length measurements and demonstrates a simple quantitative evaluation and ranking scheme for ceramic fracture based on load-adjusted crack length and cracking susceptibility. Indentation hardness and cracking threshold are also determined and related to the susceptibility. Material toughness is related to cracking susceptibility by fracture mechanics analyses: typical crack length measurements in air are shown to provide estimates of inert toughness with a relative uncertainty of ±50%.

**KEYWORDS**

cracks/cracking, fracture, fracture mechanics/toughness, hardness, indentation

## 1 | INTRODUCTION

The most common method of assessing the fracture properties of ceramics and glasses is the observation and measurement of cracks generated at sharp indentation contact impressions. Specifically, the surface traces of radial or half-penny cracks formed adjacent to Vickers indentations are commonly measured. Such cracks are perpendicular to the indented surface and hence often control the strength of the indented component. The popularity of the method stems from: (a) the minimal specimen requirements—a flat, small area of material is merely required; (b) the ease of application—gravity-loaded indentation followed by optical microscopy is usually sufficient; and (c) the simplicity of analysis—a simple, calibrated, power law

can relate measured indentation load and crack length to material toughness. The seminal indentation crack length toughness study by Anstis et al[1] nearly 40 years ago demonstrated the caveats necessary in implementing (a)-(c) above: a large enough specimen area is required to perform a sufficient number of indentations over a peak load domain wide enough to establish the applicability of the technique; inert conditions must be maintained, usually requiring a silicone oil coating of the surface to impede moisture ingress during both indentation and microscopy; and, although the power-law formulation was well anchored in fracture mechanics,[2] the calibration of the resulting indentation crack length parameter with inert toughness was really a correlation that was demonstrated to have an accuracy of about a factor of two. Nevertheless, in the intervening period,

points (a)-(c) have overwhelmed most practice and measurements, and invariably: most studies use only one or a few indentation loads and do not assess the applicability of the technique; perform measurements in moist air without regard to crack environment, and thus the modified equilibrium and fracture kinetics; and apply the "calibration" with little regard for uncertainty in either precision or accuracy. There is no doubting the power of indentation fracture techniques to elucidate the mechanical properties of brittle materials, including erosion, wear, and strength, and microstructural and environmental effects.[3,4] However, there has been no systematic study comparable in breadth to the earlier work that critically evaluates the most used technique—the measurement of indentation crack lengths in air. In order to enable and expedite the assessment of ceramic and glass fracture properties using indentations this work will present and evaluate an extensive survey of indentation crack length measurements in air.

The measurement of indentation cracks is best viewed as the central segment of an overall indentation fracture sequence and as one of the many applications of indentation fracture.[3,4] Prior to measurement, during indentation, a range of crack geometries may form depending on the material characteristics and indentation load. Indentation crack-initiation sequences, including radial, median, half-penny, lateral, and cone cracks, are detailed in a review[5] and a recent analysis.[6] Conversely, subsequent to indentation, the strength of the indented component may be measured under inert conditions, as in the seminal indentation strength-toughness study by Chantikul et al,[7] or under both inert and reactive conditions, as detailed in a recent study demonstrating multi-scale microstructural and environmental effects in ceramic fracture.[8] Measurements of crack lengths in air during the central segment of the sequence are possible as the indentation contact, based on hardness testing of metals,[9] generates a localized zone of plastic deformation beneath the contact with surrounding stabilizing residual stress field.[2] The crack lengths thus reflect a stable equilibrium configuration of the post-indentation residual stress field and the cracked material in air. (Initiation of cracks reflects unstable equilibria in the full elastic-plastic stress field during indentation.[6] Propagation of cracks in strength tests reflects unstable equilibria in the superposed fields of an applied stress and the residual stress.[7])

The stable indentation crack lengths in air reported in the evaluation here will be characterized by two attributes common with the earlier study: a wide domain of indentation loads is utilized with consequent wide range of resulting crack lengths; a large domain of materials is studied with consequent large range of crack-length behavior. Also as before, Vickers indentations were used. The majority of measurements were recorded less than one hour after indentation by a single observer using a variety of optical microscopy methods. Surface traces of cracks are reported with no distinction made between possible crack geometries. Along with new observations, some published indentation data, by the current author[10–13] and others,[14–25] are

included. The philosophy is to abide as much as possible with common practice. The goals of the evaluation are fivefold:

## 1.1 | Measurements and observations

To provide an extensive survey of statistically-meaningful measurements and observations of indentation crack lengths in air, particularly as pertains to strength of brittle materials. Specifically, the lengths of surface traces of half-penny or radial cracks[5,6] at Vickers indentation contact impressions will be surveyed as a function of indentation load; the impression dimensions and indentation fracture thresholds will also be surveyed. The data will be expressed in a common format (after appropriate conversion if necessary) to enable assessment of the breadth of observed behavior, easy intercomparison between the current data sets, and comparison with other data and models. The results of the survey in raw form, appropriate for experimentalists and critical to the survey, are presented in comprehensive detail in the Supplemental Material.

## 1.2 | Materials

To provide a clear, unbiased, direct method for comparison of materials' susceptibilities to contact fracture and deformation. In particular, the metrics of load-adjusted crack length and hardness, respectively, will be shown to provide useful scales for these phenomena and provide easily obtainable, simply understood, and physical meaningful ranking schemes for materials identification and development.

## 1.3 | Brittleness

To provide an experimental assessment of the indentation brittleness index, here expressed as the contact impression dimension required for the onset of indentation fracture—materials with smaller indices are more brittle. The conjugate "threshold" indentation loads are given in the Supplemental Material. (Such an assessment is properly the subject for dedicated threshold studies involving *in situ* acoustic[14] or optical[5] observations or *ex situ* observations,[26] but here the large amount of data from goals (1) and (2) can provide insight, consistent with the philosophy above.)

## 1.4 | Indentation fracture mechanics and toughness

To provide clear linkages to indentation fracture mechanics and interpretation of the data in terms of estimating toughness.

## 1.5 | Multi-scale effects

To provide clear examples of the effects of environment, microstructure, and stress relaxation on indentation cracking—these effects perturb the ideal indentation and map onto the nano, micro, and meso formalism developed to describe brittle fracture in the context of indentation strengths.[8] As in goal (2), these examples provide clear indications of such effects in phenomena identification and materials development. Probabilistic analyses, recently applied to strength distributions,[27] will be applied to crack length distributions to elucidate these effects. The distributions in raw form, appropriate for experimentalists, are presented in the Supplemental Material.

It is emphasized that it is not the goal of this work to develop either mechanics-based models of indentation fracture or indentation-based techniques to measure toughness, but to assess experimental measurements of indentation crack lengths.

(A)

## 2 | ANALYSIS

## 2.1 | Indentation mechanics

Vickers indentation is performed with a square diamond pyramid loaded axially onto a surface with prescribed peak load, $P$. The maximum size of the contact semi-diagonal at peak load is $a_{max}$, such that the mean-supported peak load contact pressure is $P/2a_{max}^2$. In metals, there is very little recovery on unloading of the contact impression, generated almost exclusively by plastic deformation, such that the residual impression dimension measured after indentation, $a$, is identical to that generated at peak load, $a = a_{max}$. The mean contact pressure at peak load can thus be inferred from post-indentation measurements and is termed the hardness, $H$:

$$H = P/2a^2, \tag{1}$$

and can be related to the metal yield stress.[9] If the hardness is invariant, the variation of contact diagonal with indentation load is thus:

$$a = (1/2H)^{1/2} P^{1/2}. \tag{2}$$

In ceramics, glasses, and semiconductors, there is significant recovery of the contact impression and uplift of the surrounding material on unloading, reflecting a significant component of elastic deformation during indentation.[28] The combined elastic + plastic nature of the indentation process is the origin of the residual stress field[2] and of the diversity of indentation cracking phenomena.[6] The diagonals of the Vickers contact impression recover very little on unloading, however, such that the mean contact pressure and hardness of ceramics,
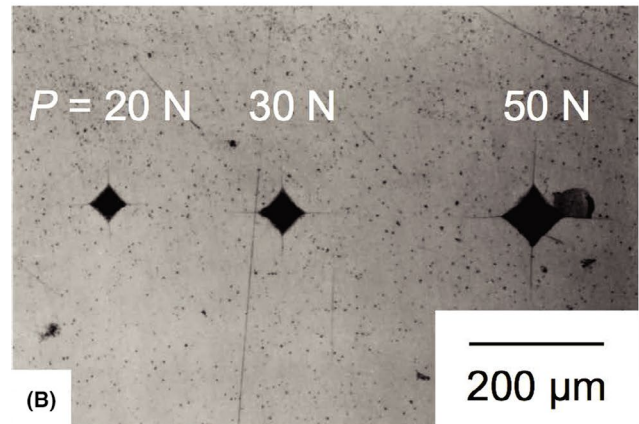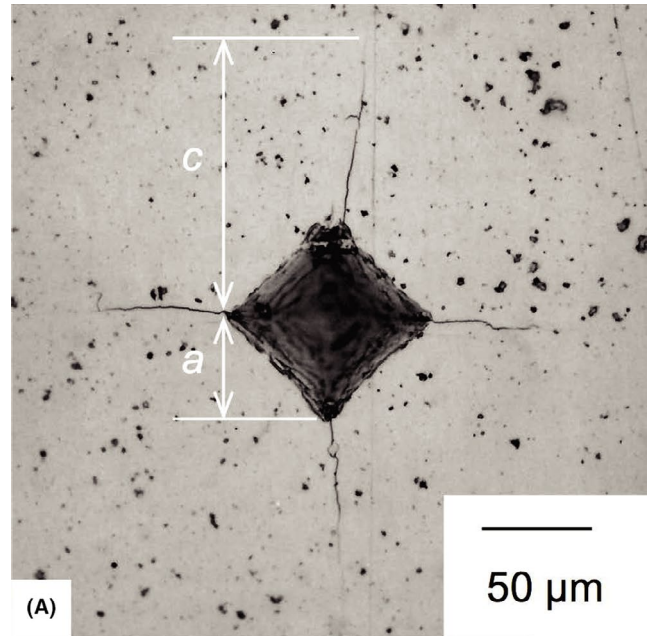
(B)

**FIGURE 1** A, Optical microscope bright-field image of a $P = 30$ N Vickers indentation in a glass-ceramic material (GC2) in air showing the contact impression size, $a$, and crack length, $c$. B, Optical image of multiple indentations in GC2 showing the increasing impression size and crack length with increasing load, and the appearance of a lateral crack chip at large load

glasses, and semiconductors can be defined by Equation (1) with the recognition that this value does not fully characterize the deformation during indentation.[6] Combinations of peak indentation loads, post-indentation impression diagonal measurements, and Equations (1) and (2) will be used here to specify hardness as a load-averaged quantity, $H = [P/2a^2]$, where $[x]$ indicates the mean value of $x$ evaluated from measurements over all indentation loads. Figure 1A shows an example of an indentation contact in a ceramic and the definition of impression dimension $a$.

The stress intensity factor (SIF) for a penny crack in an infinite continuum, center-loaded by a point force, $F$, is $K_{penny} = F/(\pi c)^{3/2}$, where $c$ is the crack radius.[29] The form of this expression is shown to be a good model for the SIF resulting from the localized loading of an indentation plastic deformation zone centered on the surface trace of a half-penny crack[2] or between two radial cracks[30] and was the form used in the earlier works.[1,7] The SIF, $K_{air}$, used here to describe the surface traces of indentation cracks in air is thus

$$K_{air} = \chi_{air} P / c^{3/2}, \tag{3}$$

where $c$ is measured from the center of the indentation impression. Figure 1A shows an example of the surface trace of an indentation crack in a ceramic and the definition of crack length $c$. $\chi_{air}$ is a dimensionless factor accounting for the subsurface geometry of the measured surface traces of the cracks and the geometry of the indentation stress field in the air environment, especially as relaxed by other cracks, for example, laterals, that extend in air.[31,32] The SIF is stabilizing as $dK_{air}/dc < 0$. Fracture equilibrium is characterized by the toughness of the material in (moist) air, $T_{air}$, such that setting $K_{air} = T_{air}$ in Equation (3) gives the stable equilibrium indentation crack length in air, $c_{air}$:

$$\chi_{air} P / c_{air}^{3/2} = T_{air}, \tag{4}$$

and thus, inverting,

$$c_{air} P^{-2/3} = (\chi_{air}/T_{air})^{2/3}. \tag{5}$$

The right side of Equation (5) involves only indenter and material parameters. If these parameters are independent of indentation load and crack length, respectively, the indentation parameter combination on the left side of Equation (5) should thus be indentation load invariant, as shown previously.[33] Following Equation 5, indentation crack lengths in air combined with peak indentation loads will thus be used here to specify individual load-adjusted crack length measurements, notated as $C = c_{air} P^{-2/3}$. Using the notation for average hardness specified above, the average load-adjusted crack length, $B = [c_{air} P^{-2/3}] = [C]$, will also be used here to specify the indentation cracking susceptibility of a material. Combining this definition and Equation (5) gives

$$c_{air} = B P^{2/3}, \tag{6}$$

which shows that indentation crack lengths should vary as $P^{2/3}$ with an amplitude, or susceptibility, of $B$. Similarly, Equation 2 shows that impression dimensions should vary as $P^{1/2}$ with amplitude $(2H)^{-1/2}$. The physical meaning of the susceptibility $B$ is that it is numerically equal to the crack length at an indentation load of $P = 1$ N, a typical minimum load in indentation crack length measurements. Figure 1B shows an example of

indentation contacts in a ceramic and the variation of indentation impression size and crack length with indentation load and the formation of lateral cracks and associated chipping and material removal at large loads.

It is possible to modify Equations (3) and (4) and thence Equation (6) to account for microstructural toughening effects and meso-scale chipping-related stress relaxation effects[10,31,32] or to use explicit radial crack models that utilize the reduced surface trace of the indentation crack, $l = (c_{air} - a)$, measured from the edge of the contact impression, most notably developed by Laugier[30] and Niihara.[34] However, here, the indentation crack length observations are viewed through the single, simple lens of Equation (5) for consistency with the earlier work and the vast majority of subsequent studies. Deviations from Equation (6) will thus be able to be compared and interpreted in terms of environmental effects, microstructural effects, stress relaxation effects, and crack geometry effects.

Another parameter that is easy to measure in indentation fracture testing is the experimental threshold load, $P_{min}$, which is the smallest indentation load at which cracks are observed. Together, the threshold and the susceptibility completely define the ideal indentation fracture response. The threshold load has a conjugate experimental threshold minimum impression dimension, $a_{min} = (P_{min}/2H)^{1/2}$. It is possible to predict these thresholds from the macroscopic indentation fracture and deformation responses by recognizing that the onset of visible cracking is marked by the condition $c_{air} = a = a^* = (P^*/2H)^{1/2}$, where the last equality defines the conjugate-predicted threshold load $P^*$ in terms of the predicted threshold impression dimension $a^*$. Using these equalities and Equations (2) and (6) gives

$$(P^*)^{1/2} / (2H)^{1/2} = B(P^*)^{2/3}, \tag{7}$$

connecting indentation fracture and deformation properties through the fracture threshold.

Equation (7) may be interpreted in two ways. The first interpretation enables between-material comparisons by establishing a relationship between material fracture and deformation properties. Rearranging Equation (7) gives

$$B = (2H)^{-1/2} (P^*)^{-1/6}, \tag{8}$$

which suggests an inverse relationship between cracking susceptibility and hardness, mediated by a very weak dependence on cracking threshold. That is, ceramic materials that exhibit substantial indentation plasticity (small hardness) should also exhibit substantial indentation fracture (large cracking susceptibility), even if large changes in threshold are observed. The measurements in this survey will provide a direct experimental test of Equation (8) and address goals (1) and (2).

The second interpretation of Equation (7) enables the between-indentation load comparison for a single material of

the predicted threshold values ($a^*$, $P^*$) with the observed values ($a_{min}$, $P_{min}$). Rearranging Equation (7) differently from above gives the thresholds predicted from the observed hardness and cracking susceptibility:

$$P^* = \left(2HB^2\right)^{-3} \tag{9a}$$

and thus

$$a^* = (2H)^{-2}B^{-3}, \tag{9b}$$

which bear some similarity to earlier analyses.[35] Deviations in crack length from Equation (6) point to indentation load-dependent variations in crack driving force, for example, stress relaxation due to large-load lateral crack growth. Similarly, deviations in crack threshold from Equation (9) point to indentation load-dependent variations in crack-initiation conditions, for example, reduced crack initiating shear fault formation at small loads.[36] The parameter $a^*$ is the indentation brittleness index,[37] here defined by direct experimental indentation plasticity and fracture observations as opposed to calculation from hardness, toughness, and assumed geometry.[37] The measurements in this survey will provide a direct experimental test of Equation (9) and address goal (3).

## 2.2 | Probability functions

The analysis above provides a set of load-adjusted crack length values through Equation 5 that enables cracks formed in the same material at different indentation loads to be compared directly. The average of this set is the susceptibility that describes the average crack length variation, encapsulated in Equation 6. The distribution of values within this set provides information regarding the nature of deviations from the average (eg, effects of environment, microstructure). The development of this distribution closely follows that recently described for ceramic strengths.[27]

An empirical distribution function (edf) was formed from the set of $N$ individual load-adjusted crack length values, $C_i$, where the index $i$ varied from 1 to $N$. The values were ranked such that the smallest and largest values of $C_i$ corresponded to $i = 1$ and $i = N$, respectively, and the conjugate quantity $Pr(i) = (i - 0.5)/N$ was assigned to each value. The discrete function $[C_i, Pr(i)]$ is then the edf, notated here as $Prob(C)$. $Prob(C)$ extends over the domain of $c_{air}P^{-2/3}$ and range of 0-1. $Prob(C)$ is the probability that a randomly selected member of the set $i$ has a load-adjusted crack length value less than $C_i$. A few earlier studies examined edf variations for raw crack lengths at selected indentation loads,[22,23] but did not test a load-dependent relationship between the crack lengths as in Equation 6. In addition, these studies assumed a complex analytical form for $Prob(C)$. Here, load-adjusted coordinates are used explicitly, and simple functional forms are used simply as smoothing functions for experimental $Prob(C)$.

The large population of all indentation crack lengths in a material is characterized by a continuous probability density function (pdf), $f(C)$, reflecting a continuous function of the indentation load- and material crack length-dependent ratio, $f(\chi_{air}/T_{air})$, Equation (5). The continuous cumulative distribution function (cdf) of the population, $F(C)$, is given by

$$F(C) = \int_0^C f(u)\,du, \tag{10a}$$

where $u$ has been used as a dummy variable in crack length integration. More usefully here, the pdf is obtained from the derivative of the cdf:

$$f(C) = dF(C)/d(C). \tag{10b}$$

The discrete values, $C_i$, are sampled from the population and thus the function $Prob(C)$ is a statistical estimator of $F(C)$. In principle, an estimate of $f(C)$ could thus be obtained from discrete differentiation of $Prob(C)$. In practice, even with the extensive data sets to be considered here, such discrete differentiation leads to overly noisy results. Hence, to aid analysis, $Prob(C)$ will be fit here by a continuous smoothing function, $H(C)$, such that $H(C) \approx Prob(C) \approx F(C)$ and thus

$$f(C) \approx dH(C)/d(C). \tag{10c}$$

Two smoothing functions will be used. Both functions are expressed in terms of $\mu$, the relative position within the $H(\mu)$ domain:

$$\mu = \frac{C - C_{min}}{C_{max} - C_{min}}, \tag{11}$$

where $C_{min}$ and $C_{max}$ are empirical fitting parameters defining the maximum and minimum limits, respectively, of the smoothing domain, $0 \leq \mu \leq 1$. The first function is a perturbed sigmoid based on the beta function, used previously in the strength analysis:[27]

$$H(\mu) = 30\left(\mu^{3p}/3 - \mu^{4p}/2 + \mu^{5p}/5\right), \tag{12}$$

where $p$ is an empirical fitting parameter of order unity that controls the sigmoid symmetry. The second function is a perturbed linear variation, based on smoothly interpolated functions:

$$h_1(\mu) = a_1\mu,$$

$$h_2(\mu) = a_2\mu + b,$$

$$h_3(\mu) = \left(a_3\mu - \mu^{a_3}\right)/\left(a_3 - 1\right),$$

$$h_4(\mu) = [h_1(\mu)^{p_1} + h_2(\mu)^{p_1}]^{1/p_1},$$

$$H(\mu) = [h_3(\mu)^{p_2} + h_4(\mu)^{p_2}]^{1/p_2}, \quad (13)$$

where $a_i$ and $b$ are empirical fitting parameters of order unity that control linearity and perturbation and $p_i$ are empirical fitting parameters that control interpolation. Both $H(\mu)$ functions in Equations (12) and (13) are bounded, such that $H(0) = 0$ and

**TABLE 1** Ceramic materials included in survey of indentation cracks in air

| Material | Source | Microstructure | Data | ID |
|---|---|---|---|---|
| WC-Co | Sandvik Hard Materials (UK) | Composite, 25 vol % Co, 0.7, 3 | Laugier (1987)[16]; Han (1990)[17] | W |
| $ZrO_2$ | Custom | Y-doped polycrystal, 0.4 | Braun (1993)[43]; Cook (1994)[11,12] | Z1 |
| $Si_3N_4$ | Commercial | Polycrystal, u | Wang (2002)[21] | SN |
| $Al_2O_3$–TiC | Custom | Composite, 30 wt % TiC, 6.8 | Gong (2001)[19] | AT1 |
| $Al_2O_3$ | Custom | MgO-doped polycrystal, 3.7 | Balakrishnan (2009)[24] | A1 |
| SiC | NC203 (Norton, Worcester, MA) | $Al_2O_3$-doped Polycrystal, 4 | Present study[38] | SC1 |
| $ZrO_2$ | Greenleaf, Saegertown, PA | Y-doped polycrystal, u | Present study | Z2 |
| $Al_2O_3$–TiC | Greenleaf, Saegertown, PA | Composite, 5 | Present study | AT2 |
| SiC | Carborundum, Niagara Falls, NY | Polycrystal, 7 | Lankford (1979)[14] | SC2 |
| $Al_2O_3$ | F99 (Friedrichsfeld, Mannheim, Germany) | Polycrystal, 6 | Present study[40,42] | A2 |
| $Al_2O_3$ | AD90 (Coors, Golden, CO) | Glass-bonded polycrystal, 4 | Present study[8,40,42] | A3 |
| $Al_2O_3$ | AD96 (Coors, Golden, CO) | Glass-bonded polycrystal, 10 | Present study[38,42] | A4 |
| Cordierite | Custom | Glass-Ceramic, 1.3 | Morena (1983)[15] | GC1 |
| $Al_2O_3$ | Custom | Glass-bonded polycrystal, 10 | Charles (2004)[22] | A5 |
| $Al_2O_3$ | Custom | $Cr_2O_3$-doped polycrystal, 20 | Present study[44] | A6 |
| Cordierite | Custom | Glass-Ceramic, 3 | Present study[8,46] | GC2 |
| $Li_2SiO_3$–$SiO_2$ | Custom | Glass-Ceramic, 41 | Present study[40–42] | GC3 |
| Glass | Custom | Cordierite composition | Morena (1983)[15] | CG |
| $Al_2O_3$ | | (0001) single crystal | Present study[8,40,42] | A7 |
| MgO | Custom | Polycrystal, 9.2 | Cook (1992)[10,45] | M1 |
| $CaTiO_3$ | 3M, St Paul, MN | SrO-doped polycrystal, 2 | Present study | CT |
| MgO | Custom | Polycrystal, 26 | Cook (1992)[10,45] | M2 |
| Tooth Enamel | Custom | Human molar, u | Padmanabhan (2010)[25] | HE |
| $BaTiO_3$ | Channel Industries, Santa Barbara, CA | Polycrystal, 7 | Present study[39] | BT1 |
| $BaTiO_3$ | K2300 (Kemet, Simpsonville, SC) | $Bi_2O_3$-doped polycrystal, u | Present study[8] | BT2 |
| Glass | | Soda-lime silicate | Charles, 2006[23] | SL1 |
| Silicon | | (001) single crystal | Tsai (1992);[18] Swadener (2002);[20] present study[13] | Si |
| MgO | | (100) single crystal | Cook (1992)[10] | M3 |
| Glass | | Soda-lime silicate | Present study | SL2 |
| (Pb, Zr)$TiO_3$ | Plessey, Australia | Polycrystal, u | Present study | PZT |

$H(1) = 1$, and both exhibit zero derivative and negative curvature at the upper bound, $H'(1) = 0$ and $H''(1) < 0$. The difference between the two functions is that, as a classic sigmoid, Equation 12 exhibits zero derivative and positive curvature at the lower bound, $H'(0) = 0$ and $H''(0) > 0$. Equation 13 encapsulates the characteristics of a heavy linear tail and exhibits the opposite behavior: positive derivative and zero curvature at the lower bound, $H'(0) > 0$ and $H''(1) = 0$. As will be seen, the perturbed linear behavior of Equation 13 describes the majority of crack length observations. In fact, in many cases, $a_1 \approx b \approx 0$, describing a single, dominant, linear trend. The fitting of Equations 11 to 13 to $Prob(C)$ observations and generation of $H(C)$ for subsequent differentiation to obtain $f(C)$ from Equation (10c) are easily performed numerically, and this was the procedure here. In many cases, $Prob(C)$ could be interpreted directly. In both cases, the analyses address goal (5).

## 3 | EXPERIMENTAL PROCEDURE

In the present study, indentation crack lengths in air were measured for a wide variety of ceramic materials, including single crystals, polycrystals, glasses, glass-ceramics, and composites. Both commercial and custom materials were included, and the characteristic microstructural scale (grain, particle, or crystallite size) varied from smaller than 1 m to larger than 20 μm; the average scale was about 5 μm. The complete data set analyzed included the extensive observations generated for the present study, significant observations previously published by others, and limited observations previously published by the author. Many of the materials included were studied in related works largely focused on strength measurements.[31,38–46] Full details, including the first author and year of previously published indentation data and references to related works, are given in Table 1, along with the material identification (ID) codes used for brevity throughout (u indicates unknown exact microstructural scale).

Materials for measurement here were polished to a reflective 1 μm diamond grit level prior to testing, except for composite $Al_2O_3$–TiC (AT2), soda-lime glass (SL2), and single crystals of $Al_2O_3$ (A7) and MgO (M3), which were tested as-received. In addition, ground surfaces of samples were removed by polishing in order to minimize compressive surface damage.[47] In many cases, more than one sample size of each material was tested in order to accommodate a wide domain of indentation loads. Samples were indented in air with Vickers diamond pyramids using six different gravity-loaded indenters with peak loads in the domain 0.1 to 500 N and dwell times of 10-30 seconds. The indentation load domain in most cases was maximized to encompass loads smaller than the cracking threshold and truncated at larger loads by excessive lateral crack damage. Except for soda-lime glass (see below), indentation impression dimensions and crack lengths were measured in air using
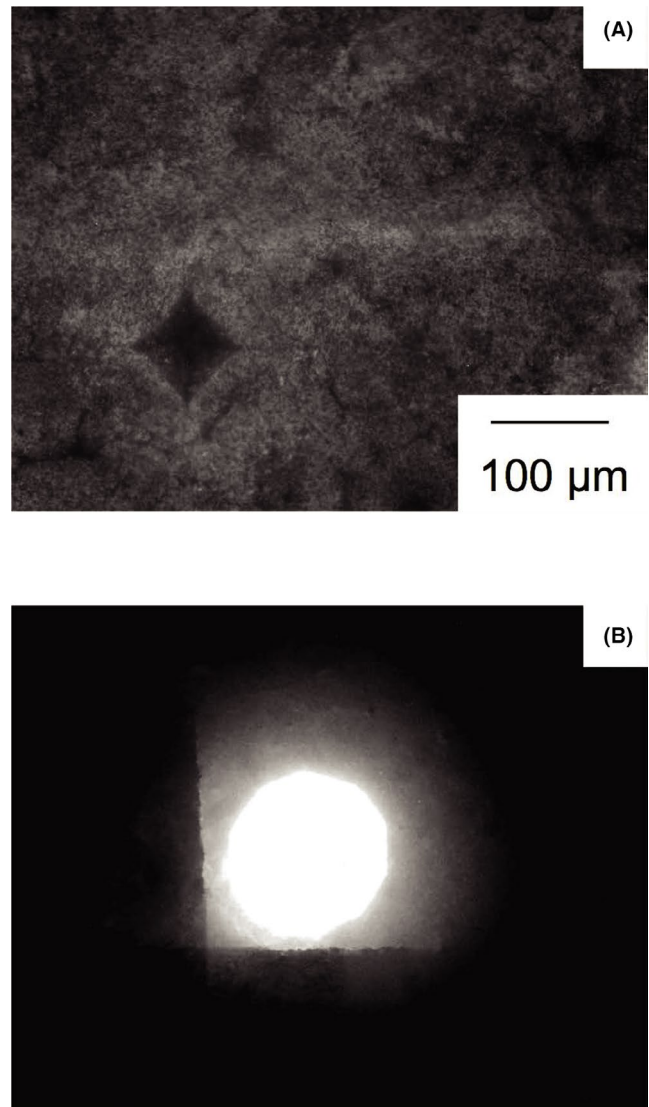


**FIGURE 2** A, Optical microscope bright-field image of a $P = 20$ N Vickers indentation in $CaTiO_3$ (CT) material; the contact impression is apparent, but the surface traces of the indentation cracks are less visible. B, Optical microscope scattered bright-field image of the same indentation and area as (A); the surface traces of the cracks are now clearly visible

optical microscopy within 1 hour of indentation. Results from all indenters were compared. No significant differences in any measured quantity were observed.

Reticles were used to calibrate at least six different optical microscopes for dimension measurements of the indentations. Lack of contrast from cracks in the usually small dielectric constant ceramic surfaces required many microscope methods, often used in combination, including bright field, dark field, polarized illumination, and Nomarski interference. By far the most effective method was scattered bright field, in which the microscope objective field aperture was partially closed and offset from the crack, leading to strong contrast across the crack plane. Similar contrast methods were used

for thermal stress-induced cracks in BaTiO$_3$.[48] An example for indentation cracks here is shown in Figure 2, in which an indentation in the CaTiO$_3$ (CT) material is shown in a conventional bright-field image, Figure 2A, with very little evidence of cracking, and in a scattered bright-field image, Figure 2B, in which the cracks are clear. Additional details of the imaging technique and images showing the effects of relative illumination position are given in the Supplemental Material, Figures S1 and S2.

In order to expand the materials domain and to ensure consistency between observations, results from selected publications were also analyzed, Table 1. Reported data were manually digitized and converted to the common format of Equation 5. In some cases the data were reported as $T_{air}$ or a related quantity,[19,21,24,25] in some cases the data were reported as the reduced crack length $l(P)$,[15] and in some cases the data were reported as the probability $Pr(c_{air})$[22,23] (see above sections for notation).

The data measured here spanned more than 20 materials and consisted in most cases of more than 100 cracks/material over a large indentation load domain. The data from the selected publications by others spanned 10 materials and were typically concentrated over a smaller load domain but with a greater number of observations/load; extreme examples were the probabilistic studies of Charles et al,[22,23] in which several hundred observations were collected for few indentation loads. In all, over 3500 indentation cracks in air from over 30 materials were analyzed here. The earlier study of Anstis et al[1] analyzed approximately 1600 cracks in inert conditions for 13 materials.

# 4 | RESULTS

## 4.1 | Indentation load variation

Figure 3 shows example results typical of a ceramic indentation crack length study, here for the CT material. The results are presented as a graph in logarithmic coordinates of indentation dimension ($a$ or $c_{air}$) vs indentation load, $P$. Both logarithmic axes extend over several orders of magnitude. To enable unbiased assessment, the graph has been drawn so that the ideal indentation crack response, a straight line of slope 2/3 in these coordinates, appears at a 45° angle to the axes (the ideal impression response is a line of slope 1/2). At the loads $P$ indicated, the solid symbols are individual measurements of $a$ and the open symbols are individual measurements of $c_{air}$. The lower solid line is a best fit to the $a$ data, consistent with Equation 2, and the upper solid line is a best fit to the $c_{air}$ data, consistent with Equation 6. Values of $H = 9.1$ GPa and $B = 15.2$ μm N$^{-2/3}$ characterize these fits; uncertainties are given in Table 2 (here and throughout, uncertainties are given as standard deviations of experimental observations).
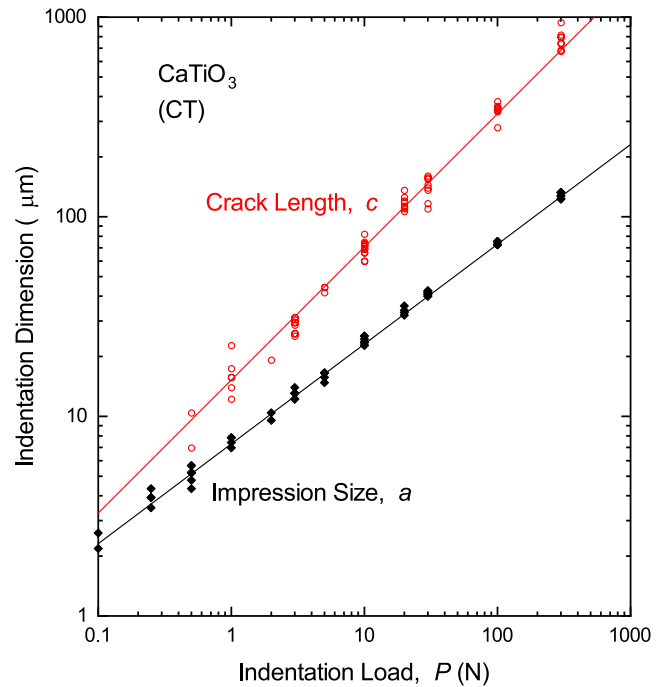


**FIGURE 3** Plot in logarithmic coordinates of the indentation dimensions, crack length, $c$, and impression size, $a$, as a function of indentation load $P$ for the CaTiO$_3$ (CT) material. Symbols are individual measurements; lines are best fits consistent with constant cracking susceptibility and hardness. Here and throughout, the crack length is that measured in air, $c = c_{air}$

The observations extend a factor of 3000 in indentation load, from 0.1 to 300 N, and the best fits describe the data over the complete load domain. Dispersion or variation about the best-fit line of the crack length measurements is greater than that of the impression dimension measurements. Cracks were not observed at the two smallest indentation loads, such that experimentally $P_{min} = 0.5$ N. The intersection of the crack length and impression size best-fit lines occurs off the graph to the left and in this case the predicted threshold load is $P^* = 0.013$ N. Similar graphs of the raw data and best fits for all 30 materials in Table 1 are given in the Supplemental Material. Graphs are all provided at the same scale (as in Figure 3, except that for WC-Co) to enable direct comparison of the extent and dispersion of the observations. Additional graphs of studies with limited indentation load domains and many observations/load are provided in expanded form. In most cases, threshold effects preclude simple interpretation or extrapolation of the best fits as predictions of observable crack lengths at very small loads, for example, $P = .1$ N or less (see below).

Figure 4 shows the edf $Prob(c)$ results determined from the data in Figure 3 using Equation 5. The results are presented in unbiased linear form as a graph extending from 0 to the maximum value in the $C$ data domain; the domain here is approximately 11 to 23 μm N$^{-2/3}$. The edf exhibits well-bounded, predominantly linear behavior with curvature

**TABLE 2** Vickers indentation deformation and fracture parameters for ceramics in air

| Material | Hardness, $H$ (GPa) | Threshold, $P_{min}$ (N) | Observations, $N$ | Cracking Susceptibility $B$ ($\mu$m N$^{-2/3}$) | Supplemental material figures |
|---|---|---|---|---|---|
| W | $15 \pm 1$ | 290 | 17 | $2.71 \pm 0.23$ | S3 |
| Z1 | $12.9 \pm 0.4$ | 20 | 97 | $5.76 \pm 0.24$ | S4(a), S4(b) |
| SN | $16 \pm 2$ | 58.8 | 365 | $6.14 \pm 0.52$ | S5(a), S5(b), S5(c) |
| AT1 | $15 \pm 2$ | 49 | 218 | $6.33 \pm 0.65$ | S6(a), S6(b), S6(c) |
| A1 | $12.7 \pm 0.8$ | 9.8 | 80 | $7.11 \pm 0.49$ | S7(a), S7(b) |
| SC1 | $26.1 \pm 2.2$ | 2 | 117 | $7.31 \pm 0.70$ | S8(a), S8(b) |
| Z2 | $13.2 \pm 0.5$ | 3 | 76 | $7.42 \pm 0.45$ | S9(a), S9(b) |
| AT2 | $20.0 \pm 1.1$ | 10 | 60 | $7.57 \pm 0.57$ | S10(a), S10(b) |
| SC2 | $30.0 \pm 4.4$ | 0.1 | 65 | $9.06 \pm 1.28$ | S11(a), S11(b) |
| A2 | $13.0 \pm 0.6$ | 3 | 64 | $9.26 \pm 1.28$ | S12(a), S12(b) |
| A3 | $16.5 \pm 0.8$ | 20 | 82 | $9.28 \pm 0.55$ | S13(a), S13(b) |
| A4 | $14.4 \pm 1.2$ | 2 | 92 | $10.2 \pm 1.1$ | S14(a), S14(b) |
| GC1 | $7.5 \pm 0.5$ | 0.54 | 34 | $10.8 \pm 1.0$ | S15 |
| A5 | $14 \pm 2$ | 2 | 114 | $12.0 \pm 3.1$ | S16(a), S16(b), S16(c) |
| A6 | $18.3 \pm 3.0$ | 0.1 | 237 | $12.1 \pm 3.8$ | S17(a), S17(b) |
| GC2 | $7.5 \pm 0.2$ | 1 | 209 | $12.9 \pm 1.1$ | S18(a), S18(b) |
| GC3 | $4.8 \pm 0.2$ | 3 | 150 | $13.0 \pm 1.4$ | S19(a), S19(b) |
| CG | $9.5 \pm 1.5$ | 0.55 | 12 | $14.2 \pm 1.8$ | S20 |
| A7 | $19.6 \pm 2.6$ | 2 | 48 | $14.4 \pm 2.5$ | S21(a), S21(b) |
| M1 | $5.7 \pm 0.4$ | 1 | 88 | $14.8 \pm 3.1$ | S22(a), S22(b) |
| CT | $9.1 \pm 1.0$ | 0.5 | 76 | $15.2 \pm 2.0$ | S23(a), S23(b) |
| M2 | $6.2 \pm 1.2$ | 0.2 | 100 | $16.0 \pm 5.3$ | S24(a), S24(b) |
| HE | $3.53 \pm 0.12$ | 0.98 | 100 | $18.2 \pm 1.0$ | S25(a), S25(b) |
| BT1 | $6.0 \pm 0.7$ | 1 | 113 | $18.5 \pm 3.0$ | S26(a), S26(b) |
| BT2 | $7.9 \pm 0.4$ | 1 | 107 | $18.7 \pm 2.8$ | S27(a), S27(b) |
| SL1 | $6 \pm 1$ | 2 | 303 | $19.6 \pm 1.4$ | S28(a), S28(b) |
| Si | $10.3 \pm 0.9$ | 0.1 | 61 | $19.9 \pm 2.1$ | S29(a), S29(b) |
| M3 | $5.9 \pm 2.2$ | 0.2 | 56 | $21.6 \pm 2.7$ | S30(a), S30(b) |
| SL2 | $5.9 \pm 0.5$ | 2 | 82 | $22.3 \pm 1.9$ | S31(a), S31(b) |
| PZT | $3.4 \pm 0.2$ | 2 | 163 | $24.4 \pm 2.2$ | S32(a), S32(b) |

and an extended tail at large values and a slight linear tail in the form of a change in derivative at small values. There is an overall concave shape; the edf is not sigmoidal. The upper bar in Figure 4 indicates the primary indicators of central tendency and dispersion of the distribution. The open symbol indicates the mean of the distribution and the box represents the standard deviation limits about the mean; the values are those given in Table 2 and the mean value corresponds to that used in Figure 3. The central line indicates the median of the distribution, in this case, barely distinguishable from the mean, and the end lines indicate the limits of the distribution, in this case, slightly skewed to greater values. The results of Figures 3 and 4 indicate that Equation 6 and the assumptions leading to it are good descriptions of

CT indentation fracture behavior, that indentation load-adjusted crack lengths for CT are almost symmetrically distributed about a central value, that the minimum limit of the crack length distribution is approximately half the maximum limit, that is, $C_{min} \approx 0.5 C_{max}$, and that the distribution is predominantly linear, perturbed by an extended tail at large values. Graphs of edf results for all ceramic materials in Table 1, leading to similar conclusions, are given in the Supplemental Material (some additional materials are included for comparison, and some limited data sets are omitted). The graphs are all provided in the same form as Figure 4 to enable direct comparison.
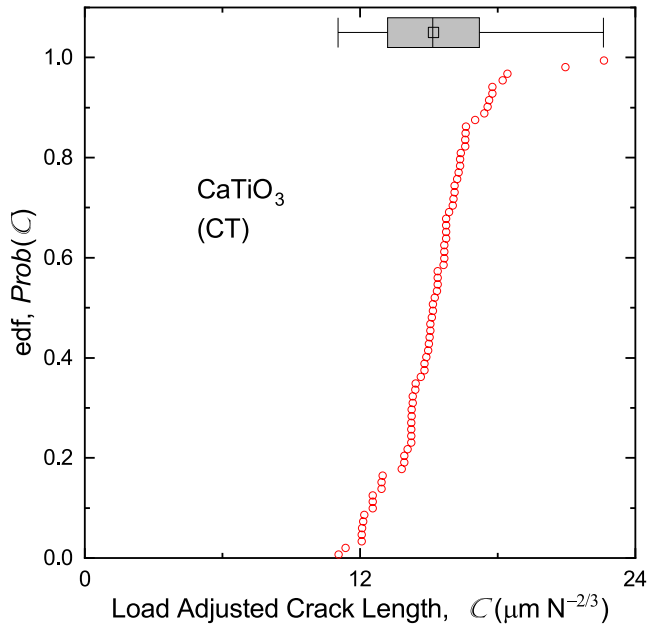
**FIGURE 4** Plot of edf, *Prob*(*C*), in terms of load-adjusted crack length, *C*, for the CaTiO$_3$ (CT) material. Symbols are individual measurements. The open symbol and shaded band represent the mean and standard deviation of the distribution; the lines and bars represent the median and bounds of the distribution

## 4.2 | Material variation

Based on the detailed raw data of the Supplemental Material, Table 2 summarizes the results of the indentation dimension analyses for the materials in Table 1 (in some cases, hardness values were determined from information provided in published works and comparison with similar materials). The materials in both Tables 1 and 2 are ranked in ascending order of mean indentation cracking susceptibility, *B*, extending from a value of 2.7 μm N$^{-2/3}$ to a value of 24 μm N$^{-2/3}$. Figure 5 is a semilogarithmic plot of the overall central tendencies and dispersions of susceptibility for the 30 materials in Tables 1 and 2 labeled by ID, using the same symbol and bar notation as Figure 4 oriented vertically.

There are many distinctive features of Figure 5. First, it is noted that the smallest value is separate from the main spectrum of values. This value represents results from the composite cermet WC-Co, making clear that this material is not a typical "ceramic" and easily distinguished by the diminished indentation cracking susceptibility. Second, the mean values for the majority ceramic materials form a continuous spectrum from about 5.5 to 24 μm N$^{-2/3}$, with relative uncertainties exhibiting no real trend and ranging from about $\pm 10\%$ to more than $\pm 40\%$. Third, the ranking reflects intuition regarding "structural" vs "functional" ceramics: zirconia, silicon nitride, and silicon carbide (Z series, SN, SC series) appear on the left of the plot with small cracking susceptibility values; soda-lime glass, barium titanate, and lead zirconate-titanate (SL series, BT series, PZT) appear on the right of the plot with large cracking susceptibility values; alumina ceramics, used in both structural and functional roles, (A series) are distributed in the center of the plot with moderate cracking susceptibility values. Fourth, the dispersions reflect intuition regarding the effects of microstructure: some of the polycrystalline Al$_2$O$_3$ (A) and MgO (M) materials with large grain sizes and, to a lesser extent, some of
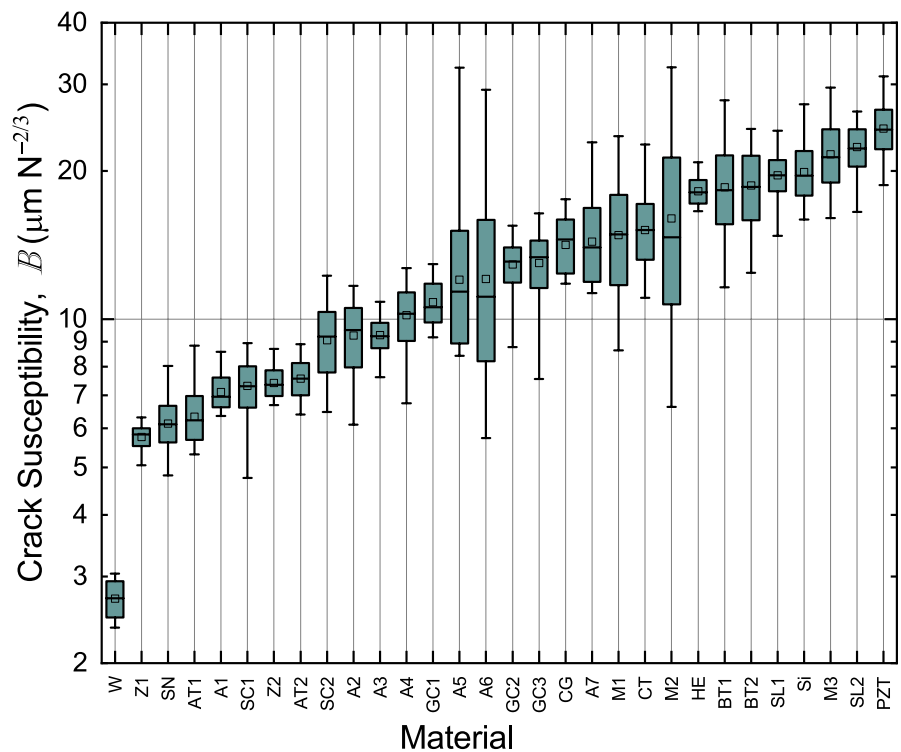


**FIGURE 5** Plot of indentation cracking susceptibility, *B*, for the 30 materials surveyed. Material identification (ID) codes given in Table 1. Susceptibility values given as mean, standard deviation, median, and bounds as in Figure 4. Materials ranked by mean value such that materials that exhibit larger cracks appear on right. Semilogarithmic coordinates

the two-phase glass-ceramics (GC) exhibit large variations in crack length and large dispersions in susceptibility.

Both the qualitative and quantitative features of Figure 5 noted above are supported by earlier observations: As with the materials analyzed here and noted previously,[1] Equation 6 is a good description of indentation cracking in WC-Co composites. Although there is considerable dependence of the observed indentation cracking susceptibility on the metallic Co content,[1,16,17,49,50] there is no doubt that the cracking susceptibility of WC-Co cermets is distinctly less than that for the main body of ceramic materials, also noted previously.[1] The large dispersions in susceptibility noted here for the large-grained polycrystals in air (A5, A6, M1, M2) were also noted earlier in inert environments.[1] Comparisons with statistically comparable data show quantitative agreement: the mean susceptibility values for soda-lime glass here, 19.6 and 22.3 $\mu m\ N^{-2/3}$, compare with 22.6 $\mu m\ N^{-2/3}$ obtained by Dabbs et al;[33] the mean susceptibility value for $Si_3N_4$ obtained here, 6.14 $\mu m\ N^{-2/3}$, compares with approximately 6.8 $\mu m\ N^{-2/3}$ obtained by Marshall;[51] the values for nearly pure, dense polycrystalline $Al_2O_3$ obtained here, 7.11 and 12.1 $\mu m\ N^{-2/3}$, compare with $(12.7 \pm 1.7)$ $\mu m\ N^{-2/3}$ and approximately 8.5 and 10 $\mu m\ N^{-2/3}$ obtained earlier;[52–54] the range of values obtained for transparent polycrystalline $Y_2O_3$ with a hardness of approximately 7.6 GPa were approximately 17 to 24 $\mu m\ N^{-2/3}$,[32] comparable to the other functional materials listed in Table 2; and the value of $(27 \pm 5)\,\mu m\,N^{-2/3}$ obtained for single-crystal $YBa_2Cu_3O_x$ compares with about 22 $\mu m\ N^{-2/3}$ for single-crystal MgO of similar hardness.[55]

Figure 6 is a logarithmic plot of $B$ vs $H$ according to Equation 8, using the data from Table 2 (solid symbols) supplemented with data from some of the above studies (open symbols).[32,51–55] The symbols and bars are means and standard deviations of the experimental observations and the lines are the slope $-1/2$ dependence of Equation 8 using $P^*$ values of 1, 0.03, and 0.001 N. The experimental observations for the wide variety of ceramic materials included are consistent with Equation 8 and almost completely described by the bounds listed. The exception to this behavior is the single point representing the composite cermet WC-Co, which displays very small cracking susceptibility relative to ceramic materials of comparable hardness. Overall, the clear positive correlation between the tendencies to plasticity and fracture at *sharp* indentations in Figure 6, consistent with Equation 8, is the exact opposite of that observed in the earlier survey by Rhee et al in which a clear *negative* correlation was observed at *blunt* (spherical) indentations,[56] reinforcing the differences between the two contact geometries.[3]

Figures 3, 4, 5, and 6, Tables 1 and 2, and the Supplemental Material completely meet goals (1) and (2) above.

Figure 7 is a logarithmic plot of the minimum impression size, $a_{min}$, at which indentation cracking was observed vs the threshold size, $a^*$, predicted using Equations 2 and 9b and the
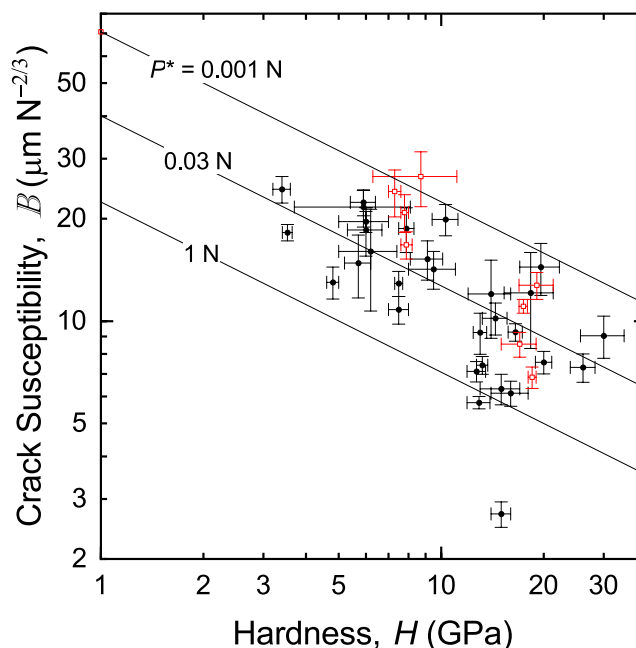


**FIGURE 6** Plot in logarithmic coordinates of indentation cracking susceptibility, $B$, vs hardness, $H$, for ceramic materials. Solid symbols represent mean experimental values of materials analyzed here; open symbols represent mean values from other studies; bars represent standard deviations. Lines represent decreasing variations with invariant cracking threshold loads $P^*$

data in Table 2. Symbols represent mean values; bars are uncertainties calculated using propagation of variance. The line represents ideal agreement. The symbol separated from the main group at large $a^*$ represents WC-Co. The conjugate plot for $P_{min}$ and $P^*$ is given in the Supplemental Material, Figure S33. The observations of Figure 7 show that the minimum impression sizes observed for the appearance of indentation cracks are much larger than the threshold sizes predicted from measured indentation cracking susceptibility and hardness. The increased sizes, by factors of 3 to 10 implied by Figure 7, are much greater than the likely overestimation of size by a factor of 1.5 introduced using discrete indentation loads separated by a typical factor of 2 (see Figure 3 and Supplemental Material). The implication is that post-indentation, large load, stable equilibrium crack configurations, as studied here (eg, Figure 3), provide only a lower bound to the nonequilibrium instability configurations at crack initiation during indentation at small loads. Specifically, Figure 7 suggests that crack nuclei decrease in potency with decreasing impression size much more rapidly than linearly, leading to significant underestimation of minimum impression sizes for cracking. The suggestion is consistent with the discrete shear faults observed to act as crack nuclei within indentation impressions,[5,36] but inconsistent with indentation crack-initiation models.[6,35]
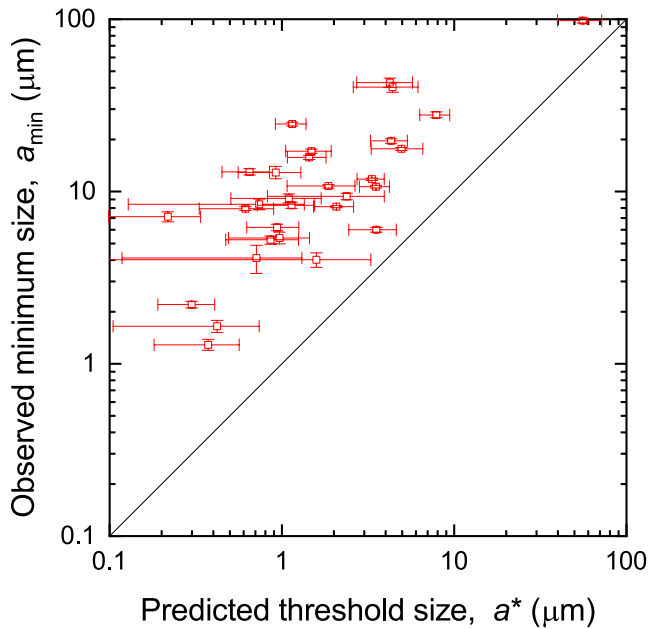
**FIGURE 7** Plot in logarithmic coordinates of minimum impression size observed for indentation cracking vs threshold impression size predicted from measured cracking susceptibility and hardness. Symbols represent mean experimental values of materials analyzed here; bars represent standard deviations determined from analysis of variance. Line represents ideal agreement

Figures 3, 4, 5, and 7, Table 2, and the Supplemental Material completely meet goal (3) above.

## 4.3 | Indentation toughness

The length of an indentation crack, $c_0$, in an unrelaxed residual stress field for a material in an inert environment is given by

$$\chi_0 P / c_0^{3/2} = T_0, \tag{14}$$

where $\chi_0$ characterizes the amplitude of the unrelaxed residual field (eg, in the absence of lateral cracking) and $T_0$ is the toughness of the material in inert conditions (eg, in the absence of reactive moisture), commonly referred to as "the toughness." In the earlier fundamental study,[1] measurements of indentation load invariant quantities $P / c_0^{3/2}$ and values of $T_0$ enabled correlation between these two fracture variables and evaluation of $\chi_0 = 0.065 \pm 0.026$, averaging over the elastic and plastic properties of the materials used. Thus, providing the conditions are met of an unrelaxed indentation stress field in an inert environment, measurements of indentation crack lengths can be used to estimate toughness within a factor of 2 using Equation 14.

In most tests in air environments, however, inert conditions are not met, which thence also leads to stress field relaxation. These effects are shown by combining Equations 4

and 14 to describe the crack length measured in toughness estimation, $c_{est}$, in a single expression.

$$c_{est} P^{-2/3} = \left( \frac{\chi_0 - \Delta\chi_{env}}{T_0 - \Delta T_{env}} \right)^{2/3}, \tag{15}$$

where $\chi_{air} = \chi_0 - \Delta\chi_{env}$, $T_{air} = T_0 - \Delta T_{env}$, and both $\Delta\chi_{env}$ and $\Delta T_{air}$ are positive and offsetting, but usually unknown. Averaging over the responses of a range of ceramic materials, inert indentation strength measurements[31] suggest that $\Delta\chi_{env} \approx 0.2\chi_0$ and reactive indentation strength measurements suggest[8] that $\Delta T_{env} \approx 0.5 T_0$, implying that $c_{est} \approx 2c_0$, consistent with observations[1,57] (strength measurements are more sensitive to these effects, see Discussion). However, the exact increase in $c_{est}/c_0$ is extremely dependent on test conditions as $\Delta\chi_{env}$ depends strongly on indentation load[13,45] and time after indentation, and $\Delta T_{env}$ depends strongly on moisture content of the environment.[57] Hence, although Equation 15 provides a scheme for consideration of indentation crack lengths in air, it cannot provide a general "correction factor" for such measurements in toughness estimation. It is likely that such a factor is greater than 1 and pertains to the accuracy with which $T_0$ can be specified, not the precision with which $c_{est} P^{-2/3}$ can be measured. For an unknown material, an upper bound to the potential error can be estimated by assuming $\Delta\chi_{env} = \Delta T_{env} = 0$, such that $c_{est}$ is assumed to be $c_0$. Equations 14 and 15 then imply that the inferred value of $T_0$ could be in error (inaccurate) by an underestimate of a factor of 3, even if the relative uncertainty (precision) in $B$ is about 0.3, as is typical, Figure 5. Further, if the midrange value of $\chi_0$ is assumed, the potential error in the estimated value of $T_0$ for an unknown material is convoluted with these environmental effects' errors by a factor of nearly 2. However, if the environmental effects' errors, $\Delta\chi_{env}$ and $\Delta T_{air}$, are shown to be comparable and small, such that $c_{est} \approx c_0$, the potential error is minimized to that associated with uncertainty in $\chi_0$.

Equations 4, 14, and 15 provide a clear fracture mechanics framework for relating commonly performed indentation crack length measurements in air to the more stringent requirements of toughness estimation. The framework meets goal (4) above and, in addition to considerations of accuracy, provides a framework for consideration of precision of measurements in air and the effects of perturbations from the ideal response. Such perturbations are considered in terms of the distributions of crack lengths in the next section.

## 4.4 | Probabilistic interpretation

It is clear from Figure 5 that the relative width and symmetry of load-adjusted crack length distributions differ between materials, an implication supported by the detailed data in the Supplemental Material. Different distributions are indicative of different perturbations from

ideal indentation cracking and provide insight into material behavior through analysis of the crack length edf. In most cases here, the overall form of the edf consisted of three sections, typified in Figure 4 by the CT material and encapsulated by Equation 13. In the first section, extending from the minimum and including small values, the response was near linear with nonzero derivative. In the second, central, section, consisting of intermediate values and dominating most observations, the response was also linear with increased derivative. The third section, including large values and extending to the maximum, exhibited negative curvature with derivative decreasing to near zero. The overall form is most easily viewed as a predominant central linear response with initial linear and final curved perturbations. In some cases, the initial linear perturbation was nearly absent (AT1, A1, Z2, AT2, A2, A5, A7, HE). In a few cases, the initial perturbation was also curved, leading to near-classic sigmoidal responses with almost zero derivative at both maximum and minimum limits (SN, SC1, GC2, GC3, SL1, SL2). In one case, the response was bimodal, consisting of two sequential sigmoidal responses (Z1, reflecting well-developed cracks and those "trapped" in a transformation zone surrounding the indentation[11,12]).

Figure 8 shows edf responses that exemplify the above cases (except for bimodal). To focus on variations in shape, the responses are plotted in normalized form using $c_{norm} = C/B$, that is, dividing the raw responses given in the Supplemental Material by the appropriate susceptibilities given in Table 2, such the edf $Prob(c_{norm})$ domain has a mean value 1.0 and typically extended from 0.5 to 1.5. Symbols represent individual crack length measurements. Lines represent best fits to the data and estimates of the cdf, $H(c_{norm})$: (a) and (b), Equation 13; (c), Equation 12. The overall responses are conveniently viewed as a sequence of perturbations: Figure 8A shows the behavior of the AT1 material, representing just over one-quarter of the cases examined. The response is dominated by a single linear variation extending from the minimum through the central mean into a curved region extending in a tail to the maximum. Figure 8B shows the behavior of the CT material, representing over half the cases examined. As in (A), the response consists of a central linear region with a curved region extending to the maximum, but that is now additionally perturbed by a linear region of reduced gradient extending from the minimum. Figure 8C shows the behavior of the GC3 material, representing just under one-quarter of the cases examined. The central linear region of (A) that was reduced in (B) is now absent, the linear perturbation about the minimum introduced in (B) is now curved, and the extended curved tail about the maximum in (A) and (B) is now reduced in extent; the cumulative perturbations generate a classic, nearly symmetric, sigmoid.

The sequence of behavior described above is made clear in conjugate pdf variations. Figure 9 shows pdf curves, $f(c_{norm})$, determined using Equation 10c and the $H(c_{norm})$ data of Figure



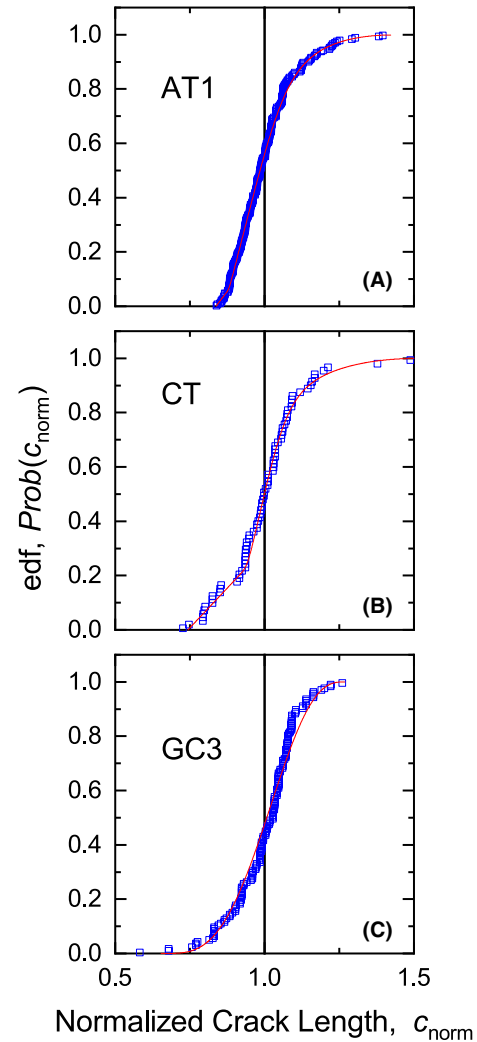**FIGURE 8** Plots of edf, $Prob(c_{norm})$ in terms of normalized crack length, $c_{norm}$, for three ceramic materials, illustrating the range of responses. A, AT1 composite, perturbed linear. B, CT polycrystal, perturbed bilinear. C, GC3 glass-ceramic, sigmoidal. The vertical lines represent the mean crack length

8. The AT1 crack density is quite asymmetric, effectively consisting of a half bell-shaped curve with mode significantly less than 1 and extending to large cracks on the right of Figure 9. The CT density is less asymmetric, with mode near 1, extending in a half bell-shaped curve to the right and including a large stepped response to the left. The GC3 density is a near-symmetric bell shape with mode near 1. The AT1 and CT responses are both "heavy tailed" at large crack lengths and narrower at small and intermediate crack lengths relative to GC3. These characteristics were common in the indentation crack distributions studied and marked by the single-value parameters of positive skewness (third moment of distribution, characterizing asymmetry) and positive kurtosis (fourth moment, characterizing heavy tails). Values are given in the Supplemental Material, Figure S34.

The interpretation of Figure 9 is as follows. During indentation the appropriate value of $T$ is $T_0$, as the indentation deformation field is overwhelmingly compressive and the indentation

event usually rapid, both factors leading to little diffusion of moisture to initiating cracks.[6] After indentation both factors are absent, and indentation cracks grow under moisture reaction- and diffusion-limited kinetics with $T_0 < K_{air} < T_{air}$, tending toward stable equilibrium at $K_{air} = T_{air}$ (Equation 4).[1,57] Measured crack lengths, $c_{air}$, thus reflect the integrated effects of fracture kinetics in varying crack driving force fields: larger driving forces cause exponentially faster cracks[8,57] and therefore generate large crack length dispersions and long-crack pdf tails, typical of the materials here, Figure 9. In many of these materials, lateral crack effects truncated or reduced the crack driving force for a small fraction of indentations, leading to reduced velocities for cracks at these indentations, and thus a fraction of short cracks marked by the stepped pdf response. In some materials, it appeared that lateral crack effects led to variable, reduced crack velocities for a much larger fraction of indentations, more than half, affecting nearly all the cracks and pdf tails at short crack lengths, leading to an overall sigmoidal response.

Based on the above, Figure 10 shows two examples of material effects on the detailed shapes of crack length distributions, beyond skewness and kurtosis. The examples include materials at two microstructural extremes: Figure 10A shows amorphous soda-lime glass (SL2) and Figure 10B shows a large-grained polycrystalline alumina (A6) that exhibited considerable crack length-dependent toughening.[44] Symbols represent individual crack length measurements. In Figure 10A, different symbols represent measurements at three different observation times after indentation (5 minutes, 18 hours, and 12 days). The surface traces of the cracks in SL2 were straight and the indentations minimally disrupted; lateral cracks only became clearly visible at the longest observation time. In Figure 10B, different
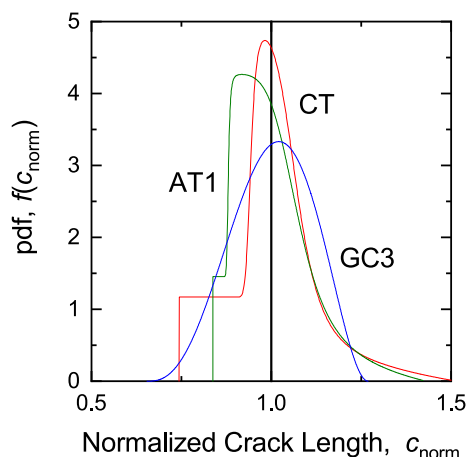
symbols represent materials with three different grain-size distributions (modal grain sizes, 10, 15, and 20 μm). The surface traces of the cracks in A6 were typically not colinear with the impression diagonals or straight and disruption of the indentation by lateral cracking, particularly at large loads, was common. At small indentation loads, the cracks were predominantly intergranular. At large indentation loads, the cracks often displayed erratic and discontinuous traces indicative of restraining traction sites.[8] In both Figure 10A,B, the solid line represents the average of the three measurements. Greater detail is shown in the Supplemental Material.

An obvious feature of Figure 10 is the difference in scale and shape of the two materials' responses. SL2 displays narrow, linear responses, perturbed at either extreme, that increase slightly in width with observation time. A6 displays wide, concave responses marked by extended long-crack tails and a short-crack linear region. The increases in width of the SL2 responses reflect the increased exposure to the environment with increased observation time and therefore greater nonequilibrium crack extension. It is notable that the extension rate decreases with time as equilibrium is approached and that there is little change in the short-crack, lateral crack suppressed, response. The solid
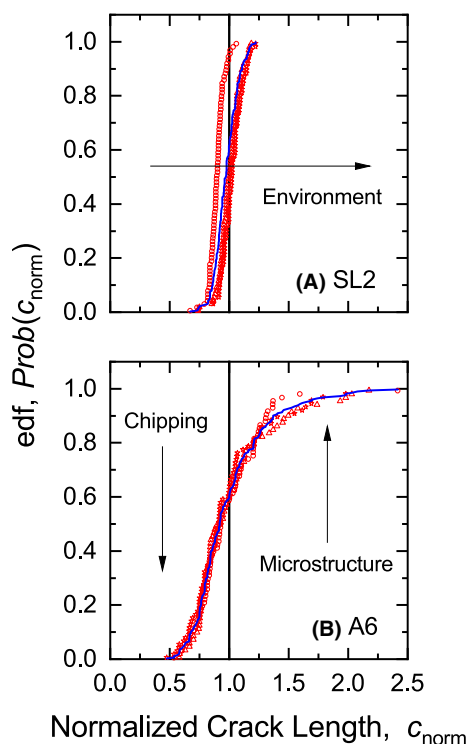


**FIGURE 9** Plots of pdf, $f(c_{norm})$ in terms of normalized crack length, $c_{norm}$, for the three ceramic materials in Figure 8, illustrating the conjugate range of responses. A, AT1 composite, asymmetric with long-crack heavy tail. B, CT polycrystal, asymmetric with long-crack heavy tail and short-crack invariant segment. C, GC3 glass-ceramic, symmetric bell shape. The vertical line represents the mean crack length



**FIGURE 10** Plots of edf, $Prob(c_{norm})$ in terms of normalized crack length, $c_{norm}$, for two materials, illustrating the effects of perturbations from the ideal response. Symbols represent individual measurements; lines represent average responses. A, SL2 soda-lime glass, broadening effect of environmental crack growth. B, A6 alumina polycrystal, broadening effects of lateral crack chipping and microstructural toughening. Details in Supplemental Material, Figures S17 and S31

line indicates the likely effect of measuring crack lengths at a broad range of times after indentation—a broadening of the edf. The similarity of the A6 responses suggests no significant effect of microstructure on indentation crack lengths (see Discussion); the solid line indicates the average response for these materials. The effects of lateral cracking and chipping are clear in the distinctive linear region at small crack lengths. The effects of microstructure are made clear by extending Equation 15 to read

$$c_{\text{est}} P^{-2/3} = \left( \frac{\chi_0 - \Delta\chi_{\text{env}}}{T_{\text{air}} + \Delta T_\mu} \right)^{2/3}, \quad (16)$$

where $T_{\text{air}}$ is the grain-boundary toughness in air. $\Delta T_\mu$ is positive and increases with crack length to reflect an increasing number of microstructurally generated restraining tractions, or, for easier interpretation here, and $\Delta T_\mu$ decreases with decreasing crack length. The extended tail in Figure 10B is thus understood to represent a large number of cracks longer than the average propagating in the reduced toughness grain boundaries and relative absence of restraining tractions characterized by reduced $\Delta T_\mu$.

# 5 | DISCUSSION

The information provided here is of direct use to those developing, assessing, and designing ceramic materials and components for mechanical applications. Specifically, the information enables the quantification and ranking of susceptibility to brittle fracture in air—the most pervasive mechanical limitation to ceramic and glass applications and the most commonly tested mechanical property. The quantification and ranking are based on the measurement of indentation cracks: the central element of the work here is an extensive survey and analysis of such crack lengths in air as a function of indentation load. The detailed raw data of the survey, provided in the Supplemental Material, exemplified in Figure 3, enable direct comparison with other experimental data and models. It is hoped and anticipated that the usefulness of the Supplemental Material will be extended by further research to add comparable data on other materials. The analysis of cracking susceptibility, leading to the ranking of Figure 5, enables direct material comparisons, including cracking variability. The combination of the cracking susceptibility with indentation hardness enables direct comparison of materials' relative tendencies to indentation fracture and deformation and direct comparison with experimental indentation fracture threshold observations, Figures 6 and 7. A new analysis method, based on load-adjusted crack length distributions provided in the Supplemental Material, exemplified in Figure 4, enables perturbations from the ideal indentation fracture response to be quantified: Material-dependent behavior, such as tendency to nonequilibrium crack growth,

lateral cracking and chipping, and microstructural toughening can be identified, Figures 8, 9, and 10. The work here is in direct succession to that in the original indentation fracture toughness evaluation.[1] A critical difference is that here the much more common testing methodology of indentation crack length measurement in air is considered.

The work here also differs philosophically from the earlier study[1] and so the elephant in the room must be addressed. The earlier study enabled comparison of fracture properties through evaluation of indentation techniques for estimation of toughness. The work here does not do this but demonstrates and advocates the comparison of fracture properties through determination of indentation cracking susceptibility. Further, the work here sidesteps the principle caveat of the original evaluation of indentation techniques for toughness estimation by removing the condition that fracture must occur under inert conditions and compares cracking behavior in the overwhelmingly common test medium of air. Apart from aligning with common practice, the methodology described here involves no variables other than those measured, no additional equations, no calibration constants, and the uncertainty in material comparisons, rather than including accuracy considerations via calibration (Type A uncertainty), is restricted to the precision of measurement (Type B). The methodology further extends the usefulness of indentation techniques[3,4] to quantitative comparison in the air environment.

It might be claimed, as discussed earlier,[4] that there are two major points of objection to this philosophy. The first point is that toughness is the equilibrium material property quantifying resistance to fracture and hence material comparisons can only be made through this parameter. Minor difficulties with this point are that equilibrium conditions are not specified and cannot easily be generalized to all materials: Equilibrium at what crack length? Equilibrium in what environment? Specification of long cracks under inert conditions is restricted to materials that can be measured this way and then provides only one equilibrium point of many (eg, the crack length-dependent toughness values of $Al_2O_3$ and $ZrO_2$ are well known). However, the major, related, difficulty with this first point is that knowledge of toughness alone is of limited use in practical applications for material comparisons. Equal knowledge of the crack driving force in a given application, quantified by the SIF, is required to specify fracture behavior, including equilibria, and thus make comparisons. For example, the SIFs acting during fracture in contact wear, tensile loading, and thermal shock have completely different dependencies on crack length and materials and component properties. As a consequence, prediction of component performance and ranking of materials behavior cannot be specified using toughness alone.

The second point of objection is that indentation techniques provide variable results, that is, the precision is weak, or provide wrong results, that is, the accuracy is weak. In

addressing this point, the results of the current study provide clear guidance. Figures 4 and 5 and Table 2, including 30 materials and over 3500 cracks, make clear that the expected level of precision in measurements of indentation crack lengths in ceramics in air, averaged over a wide range of indentation loads, is a (standard deviation/mean) ratio of approximately 0.3 and a (maximum/minimum) ratio of approximately 2. The precision of results for individual indentation loads frequently yields ratios much less than these values, although the mean and standard deviation limits at a given load may not encompass the load-averaged mean response, for example, Figure 3. Inspection of the Supplemental Material indicates a weak trend of increased dispersion with decreasing indentation load, for example, GC2, although identifying this effect was compounded with threshold effects that also decreased the number of cracks at small loads. In some cases, there were influences of lateral crack and microstructural effects, in which the mean values of crack lengths were longer than the average response at small loads and shorter than the average response at large loads, respectively, for example, M2, A6, and GC1. In these cases, the (standard deviation/mean) and (maximum/minimum) ratios were greatly increased, for example, Figures 5 and 10. Also in these cases, the perturbing influences were apparent in indentation observations and, over significant data domains, the effects of the influences were recognized as monotonic. Assessment of material influences on fracture via measurement of the above ratios was, in fact, the goal in many cases included here. (Materials with significant microstructural influences, such as Z1 and A6, were excluded from the earlier study[1] as not well-behaved.) Overall, the precision of crack length measurements in air is comparable to that determined earlier under statistically comparable inert conditions. The conclusion is that lack of precision in indentation fracture (eg, excessive measurement dispersion, nonmonotonic behavior) is a perception arising from cases of insufficient data.

Considerations of accuracy include assessments of consistency between measurements and consistency with absolute values. Consistency between measurements is assessed here in three ways. First, by the inclusion of independent data from other researchers: (a) in individual material measurement sets, W, Si;[16–18,20] (b) as complete measurement sets of materials similar to those measured here, AT1, A1, SC2, A5, SL1;[14,19,22–24] (c) as complete measurement sets of materials different from those measured here, SN, GC1, CG, HE;[15,21,25] and (d) as individual measurements, Figure 6.[51–54] Second, by examining a wide range of materials, Table 1. Third, by examining several indentation phenomena: hardness, cracking threshold, and cracking susceptibility. In every case, consistency between measurements was demonstrated: The conclusion is that Table 2, Figures 5, 6, and 7, and the detailed data in the Supplemental Material are accurate representations of indentation crack lengths in air.

Consistency with absolute values is difficult to assess as there are no independent measures of $\chi_{air}$, $\chi_0$, or $T_{air}$ and hence Equations 5 and 14 cannot be tested directly. Independent measurements of $T_0$ and $P/c_0^{3/2}$ enabled the ratio $T_0/\chi_0$ to be evaluated with relative uncertainty of $\pm 0.4$.[1] Assuming the ratio $T_{air}/\chi_{air}$ to have the same relative uncertainty and taking the typical dispersion of crack length measurements in air as $\pm 0.3$ (Figure 5) gives the combined relative uncertainty for estimating the value of $T_{air}$ as $\pm 0.5$. Hence the accuracy of indentation crack length measurements for toughness in air of an unknown material can be specified to no better than $T_{air} = 1 \pm 0.5$ MPa m$^{1/2}$ or $2 \pm 1$ MPa m$^{1/2}$ or $4 \pm 2$ MPa m$^{1/2}$, and so on. The relative uncertainty can be improved somewhat with knowledge of the elastic and plastic properties of the material, but the unknown ratio $T_{air}/T_0$ probably precludes more accurate specification of the inert toughness. In conclusion, claims regarding the (in)accuracy of indentation toughness measurements are likely not supportable.

Finally, a perhaps surprising result of the extensive survey here is the broad applicability of the $P^{2/3}$ description (Equation 5) of indentation crack surface trace length $c_{air}$ as a function of indentation load $P$. For all the materials here, nearly all examined over a wide domain of indentation loads, a $P^{2/3}$ variation was the overwhelmingly dominant behavior. The variation probably reflects the dominant underlying physics of most indentation fracture systems, that of near-point loading acting on near-circular cracks, independent of the exact subsurface radial or half-penny geometry. Over narrow domains, as discussed above, other trends can be discerned for some materials, but when viewed as part of wider load domains or broader collections of materials, these are identified as small perturbations arising from well-understood lateral crack or microstructure-related effects. $P^{2/3}$ behavior was observed in materials that were demonstrated (W, Z1)[11,49,50] or surmised (M1, M2, CG, GC1)[10,15] to exhibit radial cracking. $P^{2/3}$ cracking behavior was also observed in materials that demonstrated exhibit significant lateral crack-related strengthening effects at large loads (SC1, Si, SL2, A7),[13,40] or significant microstructure-related weakening effects at small loads (GC1, GC3),[15,41] or both (M1, M2, A6)[10,44] in indentatgion strength tests. The applied stress superimposed on an indentation during a strength test generates subcritical crack extension prior to instability and component failure.[7,8] The implication is that this extension is more sensitive to lateral crack and microstructural perturbation of the overall SIF than that at indentation alone, leading to greater indentation load-dependent effects, a finding noted earlier by Bleise and Steinbrech[54] and observed here in the microstructural variations of $Al_2O_3$ (A series), MgO (M series), and some glass-ceramics (GC3 and related materials). A related implication, also indicated in the original pair of indentation studies,[1,7] is that indentation strength tests can be more revealing than crack length measurements regarding toughness variations, and such tests should be the focus of further work in this area.

## 6 | CONCLUSIONS

Measurement of indentation crack lengths in air is an extremely effective method of assessing the fracture properties of brittle materials. The method enables a quantitative evaluation and ranking of the susceptibility to contact-induced fracture, the phenomenon most pervasive in limiting the erosion and wear resistance, strength, and reliability of ceramic, glass, and semiconductor components. Provided a sufficiently broad indentation load domain is implemented in testing, the method provides for clear appraisal of internal consistency of results, to optimize the precision of individual material assessments, and clear appraisal of consistency with other results, to optimize accuracy of material comparisons. The extensive data in the survey included here provide benchmarks for expected levels of precision and accuracy for a wide range of materials and microstructures. In particular, the load-averaged cracking susceptibility parameter is shown here to exhibit a typical relative uncertainty of approximately ±0.3 within a range of a factor of 5 in the domain of ceramic materials. Method accuracy is further enhanced by the inverse relationship observed between cracking susceptibility and indentation hardness, in broad agreement with predictions assuming an invariant cracking threshold. Observed threshold loads are considerably greater than those predicted from ideal indentation measurements, suggesting significant dependence of crack-initiation mechanics on contact impression size. Analysis of load-adjusted crack length distributions is a sensitive method of revealing perturbations from the ideal indentation response by environmental, microstructural, and stress relaxation effects. Clear fracture mechanics analyses relate measurements of indentation cracking susceptibility in air to toughness in inert conditions. The analyses suggest that countervailing effects on indentation crack length measurements in air by environment and stress relaxation may reduce the relative uncertainty in toughness estimation to typically about ±0.5. This uncertainty is associated with measurement precision in air, considered here, plus correlation accuracy in inert conditions, considered earlier.[1]

## ORCID

*Robert F. Cook* https://orcid.org/0000-0003-0422-8881

## REFERENCES

1. Anstis GR, Chantikul P, Lawn BR, Marshall DB. A critical evaluation of indentation techniques for measuring fracture toughness: I, Direct crack measurements. J Am Ceram Soc. 1981;64:533–8.
2. Lawn BR, Evans AG, Marshall DB. Elastic/plastic indentation damage in ceramics: the median/radial crack system. J Am Ceram Soc. 1980;63:574–81.
3. Lawn BR, Cook RF. Probing material properties with sharp indenters: A retrospective. J Mater Sci. 2012;47:1–22.
4. Marshall DB, Cook RF, Padture N, Oyen ML, Pajares A, Bradby J, et al. The case for indentation as an enduring and exploratory characterization tool. J Am Ceram Soc. 2015;98:2671–80.
5. Cook RF, Pharr GM. Direct observation and analysis of indentation cracking in glasses and ceramics. J Am Ceram Soc. 1990;73:787–817.
6. Cook RF. Fracture sequences during elastic-plastic indentation of brittle materials. J Mater Res. 2019;34:1633–44.
7. Chantikul P, Anstis GR, Lawn BR, Marshall DB. A critical evaluation of indentation techniques for measuring fracture toughness: II, Strength method. J Am Ceram Soc. 1981;64:539–43.
8. Cook RF. Multi-scale effects in the strength of ceramics. J Am Ceram Soc. 2015;98:2933–47.
9. Tabor D. The hardness of metals. Oxford, UK: Clarendon, 1951.
10. Cook RF, Liniger EG. Grain-size effects in the indentation fracture of MgO. J Mater Sci. 1992;27:4751–61.
11. Cook RF, Braun LM, Cannon WR. Trapped cracks at indentations: I, Experiments on yttria-tetragonal zirconia polycrystals. J Mater Sci. 1994a;29:2133–42.
12. Cook RF, Braun LM. Trapped cracks at indentations: II, Fracture mechanics model. J Mater Sci. 1994b;29:2192–204.
13. Cook RF. Strength and sharp contact fracture of silicon. J Mat Sci. 2006;41:841–72.
14. Lankford J, Davidson DL. The crack-initiation threshold in ceramic materials subject to elastic/plastic indentation. J Mat Sci. 1979;14:1662–8.
15. Morena R, Niihara K, Hasselman DPH. Effect of crystallites on surface damage and fracture behavior of a glass-ceramic. J Am Ceram Soc. 1983;66:673–82.
16. Laugier MT. Palmqvist indentation toughness in WC-Co composites. J Mater Sci Letters. 1987;6:897–900.
17. Han D, Mecholsky JJ. Fracture analysis of cobalt-bonded tungsten carbide composites. J Mater Sci. 1990;25:4949–56.
18. Tsai YL, Mecholsky JJ. Fracture mechanics description of fracture mirror formation in single crystals. Int J Fracture. 1992;57:167–92.
19. Gong J, Zhao Z, Guan Z. On the local crack resistance of $Al_2O_3$-TiC composites evaluated by direct indentation method. J Eur Ceram Soc. 2001;21:941–6.
20. Swadener JG, Nastasi M. Effect of dopants on the fracture toughness of silicon. J Mater Sci Letters. 2002;21:1363–5.
21. Wang J, Gong J, Guan Z. Variation in the indentation toughness of silicon nitride. Mater Letters. 2002;57:643–6.
22. Charles Y, Vandembroucq D, Hild F, Roux S. Material-independent crack arrest statistics. J Mech Phys Solids. 2004;52:1651–69.
23. Charles Y, Hild F, Roux S, Vandembroucq D. Material-independent crack arrest statistics: application to indentation experiments. Int J Fract. 2006;142:51–67.
24. Balakrishnan A, Panigrahi BB, Chu MC, Kim TN, Cho SJ. Microindentation fracture behavior of surface modified alumina ceramic using glass infiltration. J Mater Proc Technol. 2009;209:1783–8.

25. Padmanabhan SK, Balakrishnan A, Chu M-C, Kim TN, Cho SJ. Micro-indentation fracture behavior of human enamel. Dental Mater. 2010;26:100–4.

26. Morris DJ, Myers SB, Cook RF. Indentation crack initiation in ion-exchanged aluminosilicate glass. J Mat Sci. 2004;39:2399–410.

27. Cook RF, DelRio FW. Determination of ceramic flaw populations from component strengths. J Am Ceram Soc. 2019b;102:4794–808.

28. Oliver WC, Pharr GM. An improved technique for determining hardness and elastic modulus using load and displacement sensing indentation experiments. J Mater Res. 1992;7:1564–83.

29. Stress intensity factors handbook. Murakami Y ed. Oxford, UK: Pergamon Press, 1992.

30. Laugier MT. Palmqvist crack extension and the center-loaded penny crack analogy. J Am Ceram Soc. 1985;68:C-51-C-52.

31. Cook RF, Roach DH. The effect of lateral crack growth on the strength of contact flaws in brittle materials. J Mat Res. 1986;1:589–600.

32. Cook RF, Pascucci MR, Rhodes W. Lateral cracks and microstructural effects in the indentation of $Y_2O_3$. J Am Ceram Soc. 1990;73:1873–8.

33. Dabbs TP, Lawn BR, Kelly PL. A dynamic fatigue study of soda-lime silicate and borosilicate glasses using small scale indentation flaws. Phys Chem Glasses. 1982;23:58–66.

34. Niihara K, Morena R, Hasselman DPH. Evaluation of $K_{Ic}$ of brittle solids by the indentation method with low crack-to-indent ratios. J Mater Sci Letters. 1982;1:13–6.

35. Lawn BR, Evans AG. A model for crack initiation in elastic/plastic indentation fields. J Mater Sci. 1977;12:2195–9.

36. Lawn BR, Dabbs TP, Fairbanks CJ. Kinetics of shear-activated indentation crack initiation in soda-lime glass. J Mater Sci. 1983;18:2785–97.

37. Lawn BR, Marshall DB. Hardness, toughness, and brittleness: an indentation analysis. J Am Ceram Soc. 1979;62:347–50.

38. Multhopp H, Cook RF, Lawn BR. Universal fatigue curves for ceramics using indentation flaws. J Mater Sci Letters. 1983;2:683–4.

39. Cook RF, Freiman SW, Lawn BR, Pohanka RC. Fracture of ferroelectric ceramics. Ferroelectrics. 1983;50267–72.

40. Cook RF, Lawn BR, Fairbanks CJ. Microstructure-strength properties in ceramics: I-Effect of crack size on toughness. J Am Ceram Soc. 1985;68:604–15.

41. Cook RF, Freiman SW, Baker TL. Effect of microstructure on reliability predictions for glass-ceramics. Mater Sci Eng. 1986;77:199–212.

42. Cook RF, Fairbanks CJ, Lawn BR, Mai Y-W. Crack resistance by interfacial bridging: its role in determining strength characteristics. J Mater Res. 1987;2:345–56.

43. Braun LM, Cook RF. Effect of stress on trapped cracks in Y-TZP. In: Badwal SPS, Bannister MJ, Hannink RHJ, editor. Science and Technology of Zirconia V. Lancaster, PA: Technomic Press, 1993:386–400.

44. Cook RF, Liniger EG, Steinbrech RW, Deuerler F. Sigmoidal indentation-strength characteristics of polycrystalline alumina. J Am Ceram Soc. 1994a;77:303–14.

45. Cook RF, Liniger EG, Pascucci MR. Indentation fracture of polycrystalline cubic materials. J Hard Mater. 1994b;5:190–212.

46. Cook RF. Toughening of a cordierite glass-ceramic by compressive surface layers. J Am Ceram Soc. 2005;88:2798–808.

47. Cook RF, Lawn BR, Dabbs TP, Chantikul P. Effect of machining damage on the strength of a glass-ceramic. J Am Ceram Soc. 1981;64:C121–C122.

48. Johnson-Walls D, Drory MD, Evans AG, Marshall DB, Faber KT. Evaluation of reliability of brittle components by thermal stress testing. J Am Ceram Soc. 1985;68:363–7.

49. Shetty DK, Wright IG, Mincer PN, Clauer AH. Indentation fracture of WC-Co cermets. J Mater Sci. 1985;20:1873–82.

50. Laugier MT. Validation of the Palmqvist indentation approach to toughness determination in WC-Co composites. Ceram Int. 1989;15:121–5.

51. Marshall DB. Controlled flaws in ceramics: a comparison of Knoop and Vickers indentation. J Am Ceram Soc. 1983;66:127–31.

52. Zhao J, Stearns LC, Harmer MP, Chan HM, Miller GA, Cook RF. Mechanical behavior of alumina–silicon carbide "nanocomposites". J Am Ceram Soc. 1993;76:503–10.

53. Khan A, Chan HM, Harmer MP, Cook RF. Toughness-curve behavior of an alumina-mullite composite. J Am Ceram Soc. 1998;81:2613–23.

54. Bleise D, Steinbrech RW. Flat R-curve from stable propagation of indentation cracks in coarse-grained alumina. J Am Ceram Soc. 1994;77:315–22.

55. Cook RF, Dinger TR, Clarke DR. Fracture toughness measurements of $YBa_2Cu_3O_x$ single crystals. App Phys Letters. 1987;51:454–6.

56. Rhee Y-W, Kim H-W, Deng Y, Lawn BR. Brittle fracture versus plasticity in ceramics: a simple predictive index. J Am Ceram Soc. 2001;84:561–5.

57. Cook RF, Liniger EG. Kinetics of indentation cracking in glass. J Am Ceram Soc. 1993;76:1096–106.

## AUTHOR BIOGRAPHY

**Robert F. Cook** is a NIST Fellow at the National Institute of Standards and Technology (NIST), Gaithersburg, Maryland, USA. He received a BSc(Hons I) in physics from Monash University, Melbourne, Australia in 1981 and a PhD in physics from the University of New South Wales, Sydney, Australia in 1986, spending time as a Guest Researcher at NIST (then known as the National Bureau of Standards) in 1982 and 1984. The author of over 200 peer-reviewed publications and 14 patents, his research interests center on mechanics and mechanical properties of materials, especially brittle fracture. Recent research has focused on strength distributions and small-scale stress mapping.

## SUPPORTING INFORMATION

Additional supporting information may be found online in the Supporting Information section.